



## Ultrasound-Guided Model Predictive Control of Needle Steering in Biological Tissue

Mohsen Khadem<sup>\*,‡</sup>, Carlos Rossa<sup>\*,§</sup>, Ron S. Sloboda<sup>†,¶</sup>,  
Nawaid Usmani<sup>†,||</sup>, Mahdi Tavakoli<sup>\*\*\*</sup>

<sup>\*</sup>Department of Electrical and Computer Engineering, University of Alberta  
Edmonton, Canada

<sup>†</sup>Cross Cancer Institute and the Department of Oncology  
University of Alberta, Edmonton, Canada

In needle-based medical procedures, beveled tip flexible needles are steered inside soft tissue to reach the desired target locations. In this paper, we have developed an autonomous image-guided needle steering system that enhances targeting accuracy in needle insertion while minimizing tissue trauma. The system has three main components. First is a novel mechanics-based needle steering model that predicts needle deflection and accepts needle tip rotation as an input for needle steering. The second is a needle tip tracking system that determines needle deflection from the ultrasound images. The needle steering model employs the estimated needle deflection at the present time to predict needle tip trajectory in the future steps. The third component is a nonlinear model predictive controller (NMPC) that steers the needle inside the tissue by rotating the needle beveled tip. The MPC controller calculates control decisions based on iterative optimization of the predictions of the needle steering model. To validate the proposed ultrasound-guided needle steering system, needle insertion experiments in biological tissue phantoms are performed in two cases— with and without obstacle. The results demonstrate that our needle steering strategy guides the needle to the desired targets with the maximum error of 2.85 mm.

**Keywords:** Image-guided interventions; ultrasound images; needle steering; nonlinear model predictive control.

JMRR

### 1. Introduction

Percutaneous needle insertion is a common type of minimally invasive surgery used for diagnostic and therapeutic applications such as biopsy, drug delivery, and cancer treatment. Brachytherapy is one type of needle-based intervention used for cancer treatment. In brachytherapy, the surgeon inserts a needle into a patient's body such that radioactive seeds loaded in the needles can be

placed in or near the tumor (see Fig. 1). During insertion, imaging modalities, such as X-ray, fluoroscopy and ultrasound are used to monitor the location of the needle and the prostate. Currently, transrectal ultrasound is the primary imaging modality used for prostate brachytherapy, with transverse imaging used to help guide needles to a precise target in the prostate. The efficiency of percutaneous needle insertion procedures highly depends on accurate control of the needle tip trajectory. Considering factors such as tissue deformation and needle deflection effecting targeting accuracy and given the limited control the surgeon over the inserted needle when manipulating its base, accurate steering and prediction of the needle tip during manual insertion is difficult [1]. A robotic needle steering system which automatically steers the needle can enhance needle targeting accuracy.

In this paper, an autonomous ultrasound-guided needle steering system is developed to control the needle tip trajectory by axially rotating the needle tip. The

Received 31 July 2015; Revised 16 November 2015; Accepted 11 December 2015; Published 31 March 2016. Published in JMRR Special Issue on Image-Guided Intelligent Interventions. Guest Editors: Jayender Jagadeesan and Junichi Tokuda.

Email Addresses: <sup>‡</sup>mohsen.khadem@ualberta.ca, <sup>§</sup>rossa@ualberta.ca, <sup>¶</sup>ron.sloboda@albertahealthservices.ca, <sup>||</sup>nawaid.usmani@albertahealthservices.ca, <sup>\*\*\*</sup>mahdi.tavakoli@ualberta.ca

NOTICE: Prior to using any material contained in this paper, the users are advised to consult with the individual paper author(s) regarding the material contained in this paper, including but not limited to, their specific design(s) and recommendation(s).

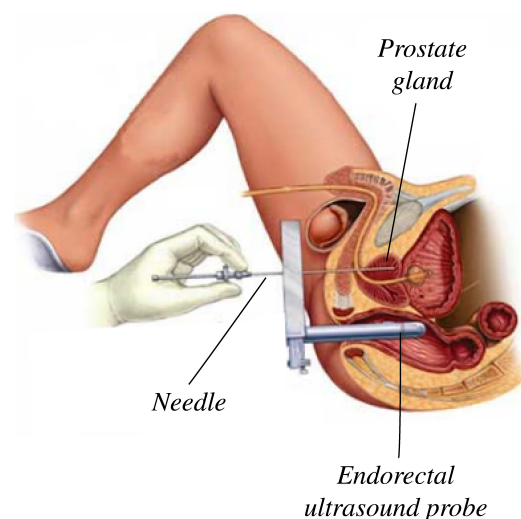


**Fig. 1.** A schematic of needle insertion in brachytherapy. The surgeon inserts long flexible needles through the patient's perineum in order to deliver radioactive seeds within the prostate gland.

control system enhances needle targeting accuracy and limits the tissue damage by minimizing number of needle rotation. The needle steering system is based on a nonlinear model predictive control (NMPC) approach. The aim of the MPC scheme is to change the actual position of the needle tip towards a desired future position following an optimal behavior. The MPC calculates control actions based on predictions of a mathematical model of needle steering. The term “needle steering” implies control of the needle tip deflection by axially rotating the needle and changing the direction of the needle tip trajectory as the needle is inserted. The model is updated online by real-time feedback of the needle tip deflection measured from the ultrasound images.

## 2. Related Work

Several needle steering strategies have been developed to allow for needle tip position adjustments during insertion [2–5]. Various inputs such as needle insertion velocity, needle axial rotation (bevel location adjustment), and needle base force/torque can be used for needle steering. The main requirement for control of needle steering is a model that relates these inputs to the needle deflection.

### 2.1. Modeling needle deflection

DiMaio and Salcudean [6, 7] and Goksel et al. [8] used the finite element method (FEM) to model the tissue interaction with a needle in order to find the needle tip position. Glozman and Shoham modeled the needle as a linear beam supported by virtual springs and used

an inverse kinematics algorithm to relate the needle deflection to base manipulations [9]. The focus of these efforts have been on steering of the needles with symmetric tip. Often in needle-based interventions, steerable flexible needles with beveled tips are used to enhance control over the needle deflection. A needle with an asymmetric beveled tip has an uneven distribution of forces at the tip, which causes the needle to deflect from a straight path. Using these needles, the surgeon can control the tip deflection by rotating the needle that changes the orientation of the bevel tip and causes the needle to bend in the opposite direction.

There has been extensive research on modeling steerable beveled tip needles. Alterovitz et al. presented a 2D FEM model of needle insertion considering the effect of the tip bevel [10]. Webster et al. developed and experimentally validated a kinematic bicycle-like model for steering of flexible bevel-tipped needles [11]. The model assumes that the needle tip follows a constant curvature path without causing large tissue deformation. Park et al. proposed an improved stochastic kinematic model by adding noise to the input parameters in the ideal kinematic model [12]. Minhas et al. presented the idea of duty cycled spinning of the needle during insertion and showed that the curvature of the needle path in the kinematics-based model can be controlled periodic needle rotation [13].

Several research groups have used classical beam theories to develop mechanics-based models of needle deflection [14–16]. Yan et al. modeled needle interaction with the tissue as a beam connected to a series of springs [14]. From our group, Lehmann et al. developed a needle insertion model using an Euler–Bernoulli beam deflecting under static force distribution profiles [17], and Khadem et al. used a dynamic beam theory to develop a model relating the needle tip position to insertion velocity [18]. Misra et al. used an energy-based formulation for a beam that is in contact with a nonlinear hyperplastic tissue to simulate needle steering [19]. Abayazid et al. extended the model to predict multiple-bending caused by needle rotation during needle insertion [20].

### 2.2. Needle steering

To the best of the authors' knowledge, the nonholonomic bicycle-like model [11] is the only model that has insertion velocity and axial needle rotation as its inputs. This model has been widely used for needle steering. Abayazid et al. modified the kinematics-based model by accounting for the tissue cutting angle and used the model for image-guided control of the needle tip deflection [20]. Rucker et al. proposed a sliding mode control based on the kinematics-based model and used it to track a desired trajectory within the tissue [3].

Patil et al. developed an automatic needle steering approach for reaching targets in 3D environments while

avoiding obstacles [4]. Their approach relies on a rapidly exploring random tree (RRT) motion planner that calculates the optimal tip trajectory using the kinematics-based model of needle steering. Vrooijink *et al.* developed a needle steering system that uses 2D ultrasound images to estimate the needle pose and an RRT motion planner that computes a feasible needle path toward the target based on the needle pose estimation. Adebar *et al.* presented a method for 3D ultrasound guidance of robotic needle steering in biological tissue. They used Doppler imaging combined with a piezo-actuated vibrating needle to track and control the needle tip [21].

The performance of the model-based controllers highly relies on accurate model predictions and precise needle position estimation. The widely used kinematic model assumes that as the needle is inserted, it moves on a constant curvature path, which is not always the case [22]. Also, the model assumes that the needle is flexible relative to the tissue and neglects the effects of tissue deformation. Previous studies have shown that when the kinematic model is applied to path planning and control in soft tissues, there are nonnegligible deviations between the model and experimental data [19, 23].

### 3. Objective

In this paper, we present a novel needle steering controller based on model predictive control theory. The goal is to steer the needle tip to follow a desired trajectory and reach a target point in the tissue. The desired tip trajectory can be a straight line toward the target location or a path around patient-specific anatomical obstacles. Obstacles are sensitive or impenetrable anatomical regions in the proximity of the target point such as glands, blood vessels or bones. Given preoperative medical images the clinician can specify the insertion location and target region as well as sensitive structures and obstacles.

Figure 2 shows a block diagram of our closed-loop control algorithm for ultrasound-based guidance of needle steering. The three main components of the

needle steering system are highlighted in Fig. 2. The first one is a novel mechanics-based needle steering model that predicts the needle deflection and accepts needle tip rotation as an input. This model is an extension of the mechanics-based needle deflection model presented in our previous work [18]. Modifications are made to account for effects of the needle rotation on the needle tip deflection.

The second component is a needle tip tracking system that estimates the needle deflection from the ultrasound images. Ultrasound image feedback is given to the model (the first component) as the initial condition in the sense that the needle steering model employs the estimated needle deflection at the present time to predict needle tip trajectory in the future steps. The third component is a NMPC that steers the needle inside the tissue by rotating the needles beveled tip. The MPC controller calculates the control decisions based on iterative optimization of a cost function. The cost function evaluates the difference between the predictions of the needle steering model and the desired tip trajectory.

Figure 3 shows the procedure used in the proposed MPC approach to find the optimal control inputs. First, the needle tip position is determined using the ultrasound images. Using the needle steering model and image-based feedback, multiple needle tip trajectories are simulated for different depths of rotation. Next, the MPC controller selects the optimal path and the corresponding depth of rotation and uses the inputs to steer the needle towards a target point.

#### 3.1. Contributions

The aim of this research is to demonstrate the feasibility of using mixed online image feedback and model predictions for optimal needle steering and increasing targeting accuracy in needle-based interventions. Our primary contribution is a novel image-guided MPC approach for steering of needles in soft tissue, which can be used to target a specific point or to follow a desired trajectory and manoeuvre the needle tip around an obstacle. Other contributions of this paper include: (1) A real-time needle steering model that predicts needle deflection based on axial rotation of needle as an input. (2) Combining online image-based needle estimation and model prediction to achieve desired needle tip trajectories. (3) Implementing an optimal image-based controller such that it not only enhances targeting accuracy but also minimizes patient operative trauma (i.e. tissue damage) by limiting the number of needle axial rotations and tissue cutting.

The rest of the paper is organized as follows: In Sec. 4, our new mechanics-based model of needle steering is presented. In Sec. 5, the process of needle tracking from ultrasound images is discussed. Details of the proposed MPC scheme are presented in Sec. 6. In Sec. 7,

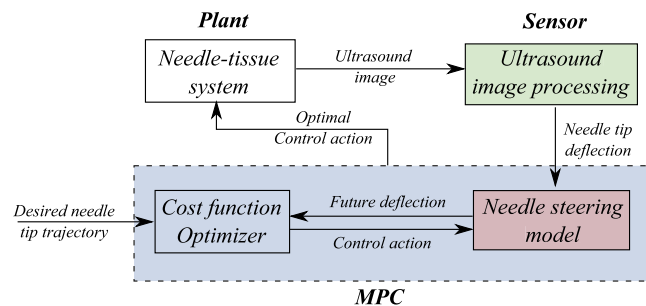
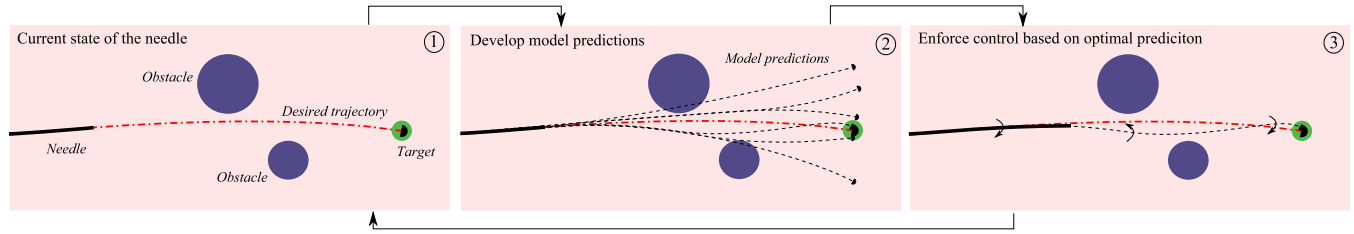


Fig. 2. Scheme of the MPC closed-loop components.



**Fig. 3.** Ultrasound-guided model predictive needle steering steps. (1) The current position of the needle tip is estimated from ultrasound images. (2) The position of needle tip is used as initial condition in the needle steering model. Since the model accepts needle axial rotation as an input, an optimization algorithm is used to generate multiple needle tip trajectories corresponding to needle rotation at various future depths. (3) The closest path to the desired trajectory that has the minimum amount of tissue deformation and the least number of needle rotations is selected as the optimal path. The control input (depth of axial rotation) corresponding to the optimal path is used to steer the needle. Since the needle tip will inevitably deviate from its model prediction because of tissue inhomogeneity and uncertainties in model parameters, the above MPC loop is repeated to continually monitor and compensate for needle tip deviations.

experiments are performed on an *ex vivo* animal tissue to validate the needle steering model, evaluate the needle tracking and steering algorithms, and demonstrate that the presented framework is applicable to clinical needle-based interventions.

#### 4. Modeling of Needle Steering

In this section, a modification of the mechanics-based needle deflection model in Ref. 18 is extended to account for the needle tip rotation and to develop a real-time needle steering model allowing axial rotation to be used as a control command for closed-loop needle steering. The proposed model simulates the dynamics of a flexible needle as the deflection of a cantilever beam under various static and dynamic loads. The external loads represent the effects of needle–tissue interactions. The model assumes that the needle bends in a plane (2D) and considers the effects of tissue deformation, tissue cutting force, and needle bevel angle on needle deflection.

##### 4.1. Mechanics-based model of needle deflection

Deflection of the flexible needle is modeled as the dynamic response of a cantilever beam under external static and dynamic loads. The external loads represent the effects of needle interaction with the surrounding environment. Figure 4 shows a schematic diagram of the proposed model of the flexible needle. The needle is clamped to the local frame ( $xy$ ) that is moving along the  $X$ -direction in global inertial frame ( $XY$ ) with velocity  $V$ . During the insertion, the needle cuts through the tissue and cutting force  $F_c$  is applied at the tip of the needle. As the needle bends tissue deforms and in turn applies forces to the needle, these forces are modeled by a transverse distributed load,  $F_s$ . This force profile is applied to the portion of the needle that is inside the tissue.

As the needle is inserted into the tissue, the location of  $F_s$  along the length of the needle changes.

The following assumptions are made in modeling the needle deflection:

- (1) The needle is inserted at a constant velocity. Also, the needle has only planar deflection and remains in the insertion plane defined by initial orientation of the needle beveled tip.
- (2) The needle behaves as a prismatic beam that is infinitely stiff in shear. Also, the rotary inertia of the needle as a result of needle bending is negligible. These assumptions are known as Euler–Bernoulli beam theory assumptions [24], which hold as long as the ratio of the beam height to the radius of curvature of the beam is much smaller than unity. This is typically the case for brachytherapy needles including the 200 mm brachytherapy needle used in our experiments, which has a slenderness ratio (needle thickness over its length) of less than 0.01.

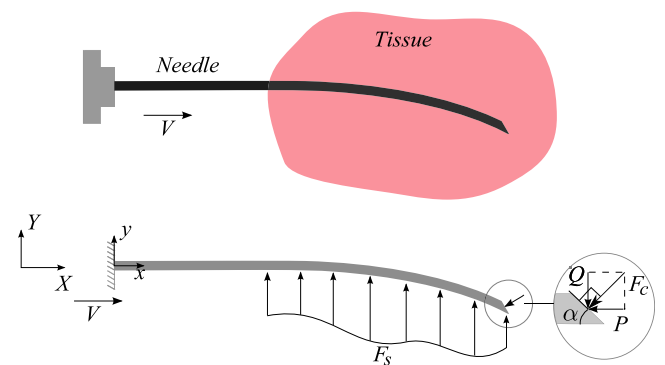


**Fig. 4.** A schematic of a bevel-tip needle inserted into a soft tissue.  $V$  is the insertion velocity,  $F_c$  is the tissue cutting force applied perpendicular to the beveled tip.  $Q$  and  $P$  are the transverse and axial component of  $F_c$ , respectively, and are related by  $P = Q \tan(\alpha)$  where  $\alpha$  is the bevel angle.  $F_s$  is the force distribution used to model tissue reaction forces as the result of its deformation caused by needle bending.



- (3) The effect of friction between the needle shaft and tissue on the needle deflection is negligible. This is a valid assumption for needle insertion in soft tissues where blood acts as a lubricant between needle shaft and tissue and reduces the magnitude of the friction force. Also, friction is an axial force tangent to the needle shaft. Assuming the axis of the beam is incompressible, effects of axial forces on bending dynamics of the beam is negligible.

Using these assumptions and following the modeling approach discussed in our previous work [18], the partial differential equation governing the dynamics of needle motion can be found as

$$EI\omega'''' + \rho A\ddot{\omega} + P\omega'' = Q\delta_\ell(x) + F_s H_{\ell-Vt}(x), \quad (1)$$

where  $\omega$  is the needle deflection, and  $E$ ,  $A$  and  $I$  are the Young's modulus, cross-sectional area, and second moment of inertia of the needle, respectively.  $Q$  and  $P$  are transverse and axial components of the cutting force, respectively (see Fig. 4). In (1), dot and prime denote differentiation with respect to time  $t$  and position  $x$ , respectively. As it was mentioned previously, the tissue force distribution  $F_s$  is a moving load acting over a specific length of the needle. Also the transverse component of the cutting force  $Q$ , is a static concentrated force acting only at the tip of the beam. In (1), in order to define the limits of these force distributions applied to a portion of the beam, we use unit step ( $H(\cdot)$ ) and Dirac delta ( $\delta(\cdot)$ ) functions defined in the  $xy$  frame as

$$\delta_{x_0}(x) = \begin{cases} +\infty & \text{if } x = x_0, \\ 0 & \text{if } x \neq x_0, \end{cases} \quad (2a)$$

$$H_{x_0}(x) = \begin{cases} 1 & \text{if } x \geq x_0, \\ 0 & \text{if } x < x_0. \end{cases} \quad (2b)$$

The needle has no deflection at  $t = 0$  and starts from rest, therefore

$$\omega(x, 0) = 0, \quad \dot{\omega}(x, 0) = 0. \quad (3)$$

The clamped side of the needle is assumed to have no deflection and have a slope of zero. The tip of the needle is assumed to experience no bending moment and the initial displacement at the tip of the needle is given by  $\omega_0$ . Thus, the following boundary conditions apply

$$\omega(0, t) = 0, \quad \omega'(0, t) = 0, \quad \omega'''(\ell, t) = 0, \quad \omega(\ell, t) = \omega_0. \quad (4)$$

Note that  $\omega_0$  is initially equal to zero. During the needle insertion,  $\omega_0$  is estimated using ultrasound images.

In the following section, a model is developed to simulate needle-tissue interaction forces. This model is implemented in (1) to develop the final model of needle steering.

## 4.2. Modeling needle-tissue interaction forces

The distributed force  $F_s$  in Fig. 4 represents the needle-tissue interaction forces. The magnitude of the approximated interaction forces are proportional to the total deformation of tissue due to the needle deflection. Taking into consideration the viscoelastic behavior of the tissue, tissue reaction forces can be related to tissue deformation using the Kelvin-Voigt model for viscoelastic tissues given by [25]

$$F_s(x, t) = K_s x_s + C_s \dot{x}_s, \quad (5)$$

where  $F_s$  is the tissue compression force around point  $x$  of the needle at time  $t$ ,  $K_s$  is the spring stiffness,  $C_s$  is the tissue damping coefficient, and  $x_s$  is the tissue deformation around point  $x$ .

In our MPC-based needle steering approach, we need to predict the needle deflection in the future steps from arbitrary and feasible initial conditions, i.e. initial deflection  $\omega_0$  at a given insertion depth  $d_0$  (see Fig. 5). In the control algorithm, the current deflection of needle tip is measured from the ultrasound images and used as feedback in closed-loop control of needle steering. Then, the developed model informed by the image feedback is used to predict the needle deflection in our desired control horizon.

Now, to calculate the tissue deformation during needle insertion, we propose a method composed of two different steps corresponding to two phases of needle-tissue interaction:

- (1) Phase 1: Needle-tissue interaction forces given initial tip deflection.
- (2) Phase 2: Needle-tissue interaction as the needle is further inserted in the tissue.

Let us define the *cutting path* as the path the needle tip cuts through in the tissue during insertion. Now, the amount of tissue deformation at the onset of insertion is the difference between the cutting path and the needle shape. Now, using the tissue model given by (5),

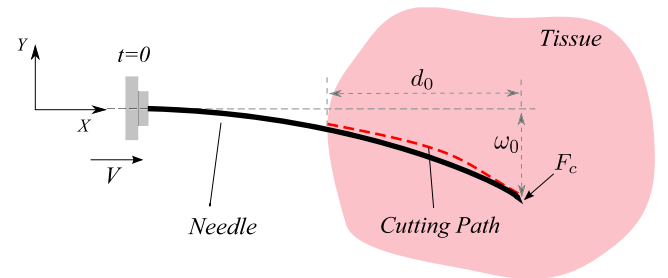


**Fig. 5.** Initial configuration of partially inserted needle in tissue.  $\omega_0$  is the initial deflection of the needle tip,  $d_0$  is the length of the part of the needle that is already inserted in the tissue, and  $F_c$  is the tissue cutting force applied to the needle tip.

needle–tissue interaction forces at the beginning of the insertion can be obtained as

$$F_{s0} = K_s[\omega(x, t) - \text{CP}(x)] + C_s\dot{\omega}(x, t), \quad (6)$$

where  $F_{s0}$  denotes the tissue forces applied to the part of the needle that is initially inserted in the tissue and CP is the cutting path. By definition, the cutting path is equal to the path followed by the needle tip. Thus, by tracking the needle tip in the incoming image frames, we can calculate the cutting path at any time instant. In the proposed image-guided needle steering approach, CP is measured from the ultrasound images and given to the model in preparation for the model-based optimization.

Now, we calculate tissue deformation forces in the second phase of needle–tissue interaction, i.e. during tissue cutting. The amount of tissue deformation is calculated by comparing the deflection of the needle element at the present time with the position of the needle tip at a certain time in past when it was in the current position of the same needle element (i.e. the cutting path). This approach is illustrated in Fig. 6. In order to find the tissue deformation at time  $t = T_2$  in the proximity of the generic point  $N$  of the needle at a position  $X_N$ , we need to find the cutting path, i.e. the needle tips transverse deflection when the tip passed  $X_N$  at time  $t = T_1$ , and subtract it from the current position of point  $N$  of the deflected needle. Then, using the spring-damper viscoelastic tissue model in (5), we can estimate needle–tissue interaction forces applied to element  $N$  of the needle.

Based on Fig. 6 and using (5), the tissue reaction force during needle steering is found as

$$F_s = K_s[\omega(x, t) - \omega(\ell, t - \tau)] + C_s\dot{\omega}(x, t), \quad (7)$$

where  $\tau$  denotes the time difference between deflection of a generic point of a needle positioned at present time

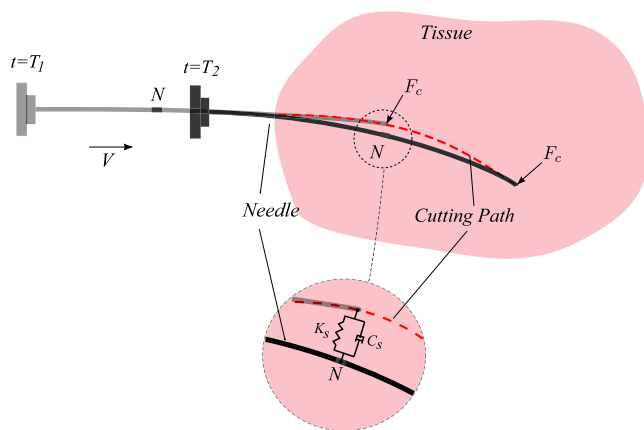


**Fig. 6.** A schematic of needle insertion and cutting path. Tissue compression around generic point  $N$  of the needle is the difference between cutting path at time  $T_1$  and deflection of the needle at point  $N$  at time  $T_2$ .  $K_s$  and  $C_s$  are the soft tissue stiffness and viscous damping coefficient.

and the cutting path (i.e. needle tip deflection) at a specific time in the past. For the point  $N$  in Fig. 6,  $\tau = T_2 - T_1$ .  $\omega(\ell, t - \tau)$  is the deflection of the needle tip or the cutting path. Assuming needle deflection is relatively small compared to the length of the needle we have

$$\tau = \frac{\ell - x}{V}, \quad (8)$$

where  $V$  is the insertion velocity.

Introducing the tissue interaction force profiles given by (6) and (7) in (1), we have the following modified model of needle steering:

$$EI\omega'''' + \rho A\ddot{\omega} + P\omega'' = Q\delta_\ell(x) + F_{s0}[H_{\ell-Vt-d_0} - H_{\ell-Vt}](x) + F_s H_{\ell-Vt}(x). \quad (9)$$

In (9), the initial needle–tissue interaction force ( $F_{s0}$ ) are only applied to the needle up to the initial insertion depth  $d_0$ , and the needle–tissue force profile for the cutting phase ( $F_s$ ) is applied to the part of the needle that passes the initial insertion depth  $d_0$ .

Note that the presented force profile enables modeling of  $180^\circ$  rotations of the needle tip and can accommodate any number of rotations. When the needle is rotated during the insertion, the orientation of the beveled tip changes as well as the direction of the transverse component of the cutting force changes, causing the needle to bend in the opposite direction and producing a double bend shape. The part of the needle that is already inside the tissue is pushed to stay in the path produced by the needle beforehand, i.e. the cutting path, restricting displacements of the elements that are already inside the tissue. Thus, the model simulates multiple bendings in the needle during needle axial rotation.

In the next section, mathematical simplification techniques are employed to reduce the order of the needle steering model in (9) for implementation in the real-time MPC.

### 4.3. Model order reduction

The PDE in (9) implies that the system has infinite dimensions. Also, the equations for calculating  $\omega$  are nonlinear and complicated to solve. Also, (9) has nonhomogeneous boundary conditions given by (4). In this section, we simplify the model to allow for real-time prediction of needle deflection.

Based on (4), we have nonhomogeneous boundary conditions. In the presence of a nonhomogeneous boundary conditions, we cannot simply solve the PDE given by (1) using conventional methods such as separation of variables or discretization techniques. In the following, we use substitution of variables to convert a nonhomogeneous boundary conditions to homogeneous. We introduce the new field variable  $\eta(x, t)$  satisfying the

following equation:

$$\omega(x, t) = \eta(x, t) + \lambda(x)\omega_0. \quad (10)$$

Substituting (10) in the boundary conditions in (4) gives

$$\begin{aligned} \eta(0, t) + \lambda(0)\omega_0 &= 0, \\ \eta'(0, t) + \lambda'(0)\omega_0 &= 0, \\ \eta'''(\ell, t) + \lambda'''(\ell)\omega_0 &= 0, \\ \eta(\ell, t) + \lambda(\ell)\omega_0 &= \omega_0. \end{aligned} \quad (11)$$

Based on (11), in order to have homogeneous boundary conditions, we must have

$$\lambda(0) = 0, \quad \lambda'(0) = 0, \quad \lambda'''(\ell) = 0, \quad \lambda(\ell) = 1. \quad (12)$$

We choose  $\lambda(x)$  as a second order polynomial satisfying (12)

$$\lambda(x) = \left(\frac{x}{\ell}\right)^2. \quad (13)$$

By substituting (13) and (10) into (9), we obtain

$$\begin{aligned} EI\eta'''' + \rho A\ddot{\eta} + P\left(\eta'' + 2\frac{\omega_0}{\ell^2}\right) \\ = Q\delta_\ell(x) + F_{s0}[H_{\ell-Vt-d_0} - H_{\ell-Vt}](x) \\ + F_s H_{\ell-Vt}(x) \end{aligned} \quad (14)$$

with the following homogeneous boundary conditions:

$$\eta(0, t) = 0, \quad \eta'(0, t) = 0, \quad \eta'''(\ell, t) = 0, \quad \eta(\ell, t) = 0. \quad (15)$$

Note that  $\eta(x, t)$  calculated using the above procedure is not a unique function. However, the solution of the original model in (9) can be correctly determined by (14).

Now, the continuous infinite-dimensional PDE model in (1) can be simplified by a mathematical discretization method. In the following, we use an approach known as Bubnov–Galerkin method [26].  $\eta(x, t)$  is approximated by a linear combination of  $n$  arbitrarily assumed functions  $W_i(x)$ ,  $i = 1, \dots, n$ , representing the first  $n$  modes of vibration. These functions satisfy the boundary conditions and are differentiable to the highest order of the PDE. Following this approach,  $\eta(x, t)$  is approximated by

$$\eta(x, t) \simeq \hat{\eta}(x, t) = \sum_{i=1}^n \phi_i(t) W_i(x), \quad (16)$$

where  $\phi_i(t)$  ( $i = 1, \dots, n$ ) are generalized coordinates expressing the deformation of the beam with respect to time. Following the Bubnov–Galerkin method, we can get a finite-dimensional approximation of the original PDE by [18]

$$\hat{\mathbf{M}}\ddot{\boldsymbol{\phi}} + \hat{\mathbf{K}}\boldsymbol{\phi} + \hat{\mathbf{R}}\boldsymbol{\phi} = \hat{\mathbf{S}}(\boldsymbol{\phi}) + \hat{\mathbf{V}} + \hat{\mathbf{G}}, \quad (17)$$

where  $\boldsymbol{\phi}$  is the vector of the generalized coordinates, and the elements of matrices and vectors in (17) are given by

$$\hat{\mathbf{M}}_{ij} = \rho A \int_0^\ell W_j(x) W_i(x) dx, \quad (18a)$$

$$\hat{\mathbf{K}}_{ij} = EI \int_0^\ell W_j''''(x) W_i(x) dx, \quad (18b)$$

$$\hat{\mathbf{R}}_{ij} = P \int_0^\ell W_j''(x) W_i(x) dx, \quad (18c)$$

$$\hat{\mathbf{S}}_i = \int_{\ell-X}^\ell F_s(x, t) W_i(x) dx + \int_{\ell-X-d_0}^{\ell-X} F_{s0}(x, t) W_i(x) dx, \quad (18d)$$

$$\hat{\mathbf{V}}_i = Q, \quad (18e)$$

$$\hat{\mathbf{G}}_i = -2P \frac{\omega_0}{\ell^2} \int_0^\ell W_i(x) dx. \quad (18f)$$

A good choice for the assumed functions ( $W_i(x)$ ) are the mode shapes of a homogenous clamped-free beam. In this way, we ensure that the assumed functions satisfy the boundary conditions in (15). The mode shapes for the clamped-free beam are given by [27]

$$\begin{aligned} W_i(x) = \frac{1}{\kappa_i} \left[ -\gamma_i \left( \cos\left(\frac{\beta_i x}{\ell}\right) - \cosh\left(\frac{\beta_i x}{\ell}\right) \right) \right. \\ \left. + \sin\left(\frac{\beta_i x}{\ell}\right) - \sinh\left(\frac{\beta_i x}{\ell}\right) \right], \end{aligned} \quad (19)$$

where  $\beta_i$  ( $i = 1, \dots, n$ ) is a dimensionless constant corresponding to different modes of vibration. In this work, we will estimate the continuous model given in (14) using the first four modes. The values of the first four  $\beta$  for a clamped-free beam are 1.857, 4.694, 7.855 and 10.996, respectively [27].  $\gamma$  and  $\kappa$  in (19) are given by

$$\gamma_i = \frac{\sin \beta_i + \sinh \beta_i}{\cos \beta_i + \cosh \beta_i}, \quad (20)$$

$$\kappa_i = -\gamma_i(\cos \beta_i - \cosh \beta_i) + \sin \beta_i - \sinh \beta_i.$$

By solving the above system of ODEs, the time functions ( $\phi_i(t)$ ) are found and the deflection of the needle at each point ( $\omega(x, t)$ ) can be calculated using (16) and (10). The matrices  $\hat{\mathbf{M}}$  and  $\hat{\mathbf{K}}$  are associated with the kinetic energy of the system and the elastic linear forces in the beam, respectively. They are both time invariant, positive definite, and symmetric.  $\hat{\mathbf{R}}$  corresponds to the non-conservative axial force  $P$ .  $\hat{\mathbf{S}}$  in (17) shows the effects of reaction forces from the tissue and can be calculated by introducing (16) and (10) in the soft tissue model given by (6) and (7).

## 5. Needle Tracking in Ultrasound Images

In this section, a method for estimating the needle tip trajectory from ultrasound images is presented. The

needle tip location and cutting path are estimated based on partial observations of the needle axial cross sections within a small region of 2D transverse ultrasound images. As discussed in Sec. 4.2, the cutting path represents the history of the needle tip deflections from the beginning of insertion up to the current time. Thus, by locating the tip position, we can also estimate the cutting path.

Researchers have previously developed needle detection algorithms using 3D volumetric images [28–30]. For instance, Ding *et al.* developed a 3D segmentation algorithm for locating the needle and implanted seeds in brachytherapy procedures [31]. Uhercik *et al.* proposed a method for detecting the position and orientation of long surgical tools in 3D ultrasound images using Random Sample Consensus (RANSAC) algorithm [32]. Zhao *et al.* implemented a Kalman filter technique in RANSAC algorithm for tracking micro-tools in 3D [31]. Tracking needle trajectory in 3D ultrasound images is computationally less efficient compared to 2D needle tracking. Also, state-of-the-art 3D ultrasound machines are very costly and not available in most of the hospitals. Thus, it is more convenient to use 2D ultrasound images for needle tracking especially for real-time applications. In needle-based medical procedures, 2D ultrasound imaging can be used to acquire transverse and sagittal images. The planes are defined in reference to the anatomical planes of the human body. In the transverse images, an axial cross section of the needle can be detected and in sagittal images a small portion of the needle shaft is visible.

Previous efforts in detecting needle tip in 2D sagittal images include the work performed by Okazawa *et al.*, who proposed a Hough transform-based detection scheme [33]. Kaya *et al.* used Gabor filtering and the utilization of RANSAC to improve needle segmentation [34]. From our group, Carrier *et al.* used RANSAC processing in combination with a simple mechanics-based needle model to predict the entire needle shape using partial observation of needle in 2D ultrasound images [35]. In brachytherapy, aligning the US probe with the sagittal plane that contains the needle is not always possible using endorectal probes.

Recently, researchers have developed needle tip detection strategies for tip tracking in 2D transverse ultrasound images. Transverse ultrasound images eliminate complications with probe alignment found in sagittal imaging. Vrooijink *et al.* presented a method for online flexible needle tracking in 3D using 2D ultrasound images [5]. They used a combination of median filtering, thresholding, and Hough transform to find the center of the needle cross section in transverse images visualizing the needle tip. Abayazid *et al.* also used 2D ultrasound to estimate needle tip pose and track the needle tip in 3D during the insertion [36]. From our group, Waine *et al.* used images from an ultrasound probe moving along the shaft of an inserted needle to estimate needle tip deflection

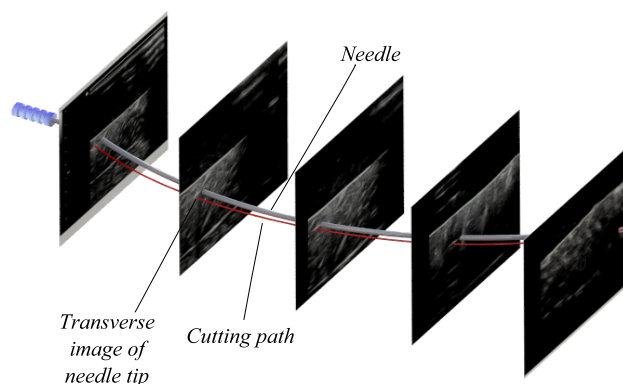


**Fig. 7.** Ultrasound-based needle tracking. Multiple transverse images of needle tip are obtained and used to reconstruct the needle tip trajectory (cutting path) in real-time.

[37]. In this approach, possible needle locations are identified in the image using a mix of filtering and thresholding. Later, RANSAC algorithm is used to find the needle tip position and predict the needle shape.

Below, we propose a new approach to track the needle tip trajectory and estimate the cutting path using 2D transverse images. Several consecutive image processing steps are combined to determine the needle tip location in each of the transverse images and to construct the tissue cutting path (see Fig. 7). In prostate brachytherapy, transverse images of needle close to the tip are acquired by inserting the endorectal probe as shown in Fig. 1. Here, we use a robotically driven ultrasound probe that follows the needle tip to capture real-time transverse images of the needle. Details of the experimental setup used to capture transverse images of the needle tip is discussed in Sec. 7.

Here is our proposed algorithm for needle tip tracking:

#### Algorithm 5.1.

- (1) A region of interest (ROI) around the initial position of the needle tip in the first frame of the ultrasound images is selected manually (Fig. 8(b)).
- (2) The selected ROI is processed using a series of image processing techniques including median filtering and iterative thresholding to reduce image noise and separate the needle tip from the image background (Fig. 8(c)).
- (3) SUSAN corner detection algorithm [38] is used to find centroid of the needle axial cross-section in the ROI (Fig. 8(d)).
- (4) A motion vector estimation algorithm is used to estimate 2D translational motion of the needle tip in the transverse images. The results are extrapolated to predict the position of the ROI in the next frame (Figs. 8(e) and 8(f)). The algorithm is repeated from step 2 using the selected ROI.



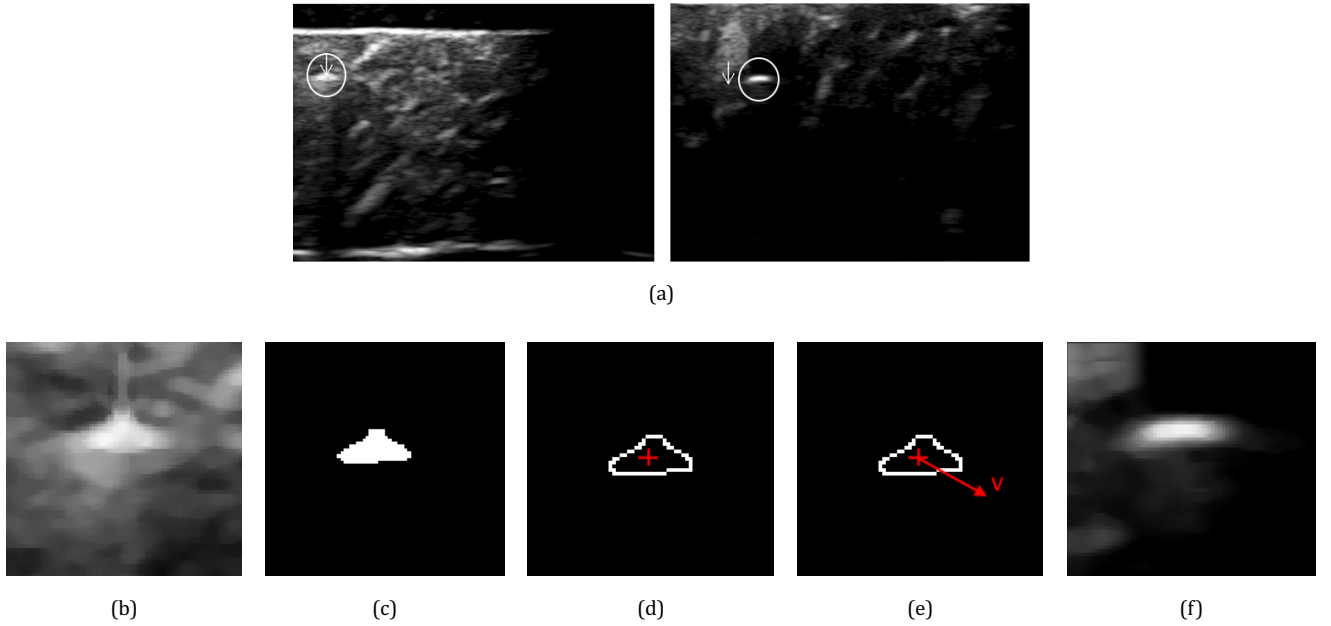


**Fig. 8.** The image processing algorithm for locating the needle tip. (a) Two subsequent transverse ultrasound images in which needle is circled in white and the position of the needle in the first frame is shown with an arrow. (b) The region of interest in the first frame is selected around the needle tip. (c) The grayscale image is smoothed to filter out the artifacts and iterative thresholding is performed to separate the needle cross section from image background. (d) SUSAN corner detection is applied and the needle tip centroid (needle tip deflection) is calculated in the selected ROI. (e) The motion vector of the needle tip in the transverse images is calculated by minimizing the sum of squared differences between the current ROI and the one from the previous frame. (f) The motion vector is used to select the ROI in the next frame.

Figure 8 shows how the image processing algorithm is applied to determine the needle tip position. After manually selecting a window of  $75 \times 75$  pixels around the initial position of the needle in the first frame, median filtering and thresholding are used to reduce speckles and eliminate small artifacts in the ultrasound image. For thresholding the image inside this ROI, first we select an initial value  $T$  for the threshold and the image is segmented. This produces two groups of pixels consisting of pixels with gray level values bigger and smaller than  $T$ . Next, the averaged gray level for the pixels in two groups are computed and used as the next value of the threshold  $T$ . This process is continued until the differences in  $T$  between different iterations is smaller than a predefined threshold.

As mentioned previously, the Smallest Unvalue Segment Assimilating Nucleus (SUSAN) edge detector is used to estimate the position of the needle cross section's centroid [38]. Following the SUSAN algorithm, a circular mask is placed around a pixel in the ROI; this pixel is called the nucleus. Next, the number of the pixels within the circular mask that have similar brightness to the nucleus are calculated. These pixels define the unvalue segment assimilating nucleus or USAN. Later the USAN size is compared to the geometric threshold to produce an edge strength image. Geometric threshold is usually chosen as  $3/4$  and  $2/3$  of maximum size of USAN for detecting edges and corners, respectively. Finally, we

select a nucleus that has the maximum size of USAN and is placed within the edges estimated using the SUSAN method as the needle tip centroid. An advantage of this method compared to other corner detectors is that SUSAN does not use the derivatives operator, which makes it faster and less sensitive to noise. Also, we select a circular template with the diameter of 21 pixels which is almost equal to the outer diameter of the needle (1.27 mm). By incorporating a geometrically exact template in SUSAN algorithm, we ensure that the algorithm selects the biggest blob that matches the needle shape rather than selecting the comet tail artifacts (CAT) commonly seen in the ultrasound images [36].

In the final step, we estimate the motion vector of the needle in 2D images to select the next ROI. The motion vector is calculated between two adjacent frames and only used to select the ROI in the upcoming frame. Under the assumption that all pixels in the ROI undergo a translational motion denoted by one 2D motion vector, we can estimate the motion vector by minimizing the sum of squared differences (SSD) between the two displaced frames. The SSD is given by

$$\text{SSD}(\mu, \nu) = \sum_{x,y} [I(x + \varepsilon, y + \nu) - I(x, y)]^2, \quad (21)$$

where the pixel intensity at position  $(x, y)$  is given by  $I(x, y)$  and  $\varepsilon$  and  $\nu$  are components of motion vector in the  $x$  and  $y$  directions, respectively.

In order to calculate the motion vector, a fast template search algorithm is presented. In this method, we search between neighboring pixels of the centroid in the current frame to find the pixel in which the sum of squared differences (SSD) between the current and previous frames is minimum. In the fast search algorithm, first a  $20 \times 20$  window of pixels around the located needle tip is selected. Then, we simply move the center of the template on 16 randomly selected neighboring pixels and calculate the SSD over the whole area spanned by the template. The pixel in which the magnitude of SSD is minimum is selected as the new centroid. Next, we accelerate the algorithm by cutting down the search step size by two and repeat the search around the newly selected centroid. The search is continued until the search step becomes one. Finally, the motion of the newly found matched template is equal to  $(\varepsilon, \nu)$  in (21).

After the needle tip position is determined, the cutting path can be estimated by fitting a third order polynomial to the tip position using the linear least squares method. Each pixel in the ultrasound image is 0.063 mm. This is the maximum accuracy for estimating the cutting path. However, considering the error of image processing and needle tracking, this error can be larger. The cutting path and current needle tip position will be used as the feedback in the closed-loop control of needle steering discussed in the next section.

## 6. MPC for Needle Steering

MPC is an advanced optimal control technique widely applied in the area of process industry [39]. The main advantage of MPC is its simplicity to define and handle constraints. MPC uses the discrete model of the process (e.g. needle steering) in order to predict and optimize the future behavior of the system as shown in Fig. 2. Given the last measurement available at the present time ( $t_n$ ), the controller predicts the dynamic behavior of the system over the horizon  $N$  based on the model of the system. Only the first element of the predicted optimal input sequence is applied to the plant until the next measurement is available. Subsequently, the horizon is shifted one step forward and a new optimization problem is formulated and solved [40]. In our case, the control input is a binary signal corresponding to  $180^\circ$  axial rotation of the needle.

We can discretize the needle steering model given by (17), (16) and (10) as

$$\omega_u(k+1) = f(\text{CP}, \omega_0, \omega_u(k), u(k)), \quad k = 0, \dots, N-1. \quad (22)$$

Using (22), we obtain predictions  $\omega_u(k+1)$  for the deflection of the needle tip at the time  $t_{n+k}$  in the future. In (22),  $f$  is our model that gives the future needle

deflection  $\omega_u(k+1)$  as the function of the current control value  $u(k)$  and the current needle deflection  $\omega(k)$ . The cutting path CP and the initial tip deflection  $\omega_0$  are the initial conditions for solving  $f$ . CP and  $\omega_0$  are obtained from the ultrasound images as discussed in Sec. 5. Starting from the current state  $\omega(n)$ , for any given control sequence  $u(0), \dots, u(N-1)$  over the horizon length  $N \geq 2$ , we can now use (22) to construct the prediction trajectory  $\omega_u$ .

Next, we use optimal control in order to determine  $u(0), \dots, u(N-1)$  such that  $\omega_u$  is as close as possible to our desired trajectory  $\omega_d$ . To this end, we define a cost function  $\mathcal{L}(\omega_u(k), u(k))$  that depends on the distance between  $\omega_u(k)$  and  $\omega_d = 0$  for  $u(0), \dots, u(N-1)$ . Here, we not only allow for penalizing the deviation of the output from the reference but also the distance of the control values  $u(k)$  to a reference control  $u_d$ , which here we choose as  $u_d$ . By penalizing  $u(k)$ , we can minimize the number of needle rotations and limit the amount of tissue cutting during the insertion. A common and popular choice for this purpose is the quadratic function

$$\mathcal{L}(\omega_u, u) = \|\omega - \omega_d(n)\|^2 + \Lambda \|u\|^2, \quad (23)$$

where  $\|\cdot\|$  denotes the Euclidean norm and  $\Lambda$  is a weighting parameter that penalizes the control action. The optimal control problem now becomes

$$\text{minimize } \mathcal{J}(n, \omega(n), u(0)) = \sum_{k=0}^{N-1} \mathcal{L}(n+k, \omega_u(k), u(k)) \quad (24)$$

with respect to all admissible control sequences  $u(0), \dots, u(N-1)$  with  $\omega_u$  found from (22).

Let us assume that this optimal control problem has a solution given by  $u^*(0), \dots, u^*(N-1)$ , where  $*$  denotes the internal optimal control variable. In order to get the desired feedback value  $\mu_n$  at  $t_n$ , we now set  $\mu_n := u^*(0)$ , i.e. we apply the first element of the optimal control sequence. This procedure is sketched in Fig. 9. At the

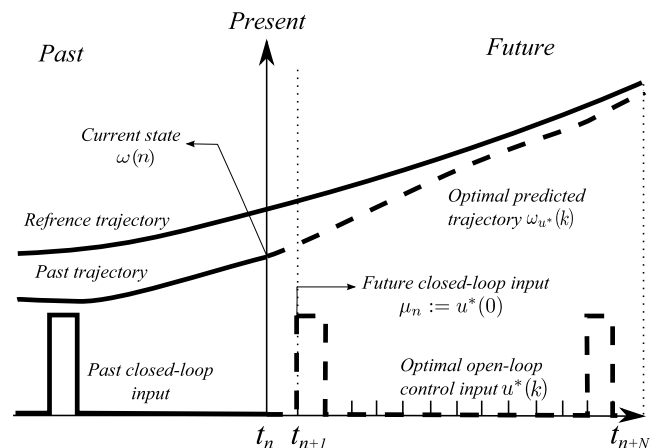


Fig. 9. Illustration of the MPC step at time  $t_n$ .

following time instants  $t_{n+1}, t_{n+2}, \dots$ , we repeat the procedure with the new ultrasound-based measurements at  $\omega(n+1), \omega(n+2), \dots$ , in order to derive the feedback values  $\mu_{n+1}, \mu_{n+2}, \dots$ . In other words, we obtain the feedback law  $\mu$  by an iterative online optimization of our model predictions over a moving horizon.

In the following section, details of NMPC algorithm are discussed. The additional term “nonlinear” indicates that our model is not a linear map.

### 6.1. Model predictive algorithm

The NMPC algorithm for constrained control of needle tip trajectory for tracking a desired time varying trajectory at each sampling time  $t_n$ ,  $n = 0, 1, 2, \dots$ , is:

#### Algorithm 6.1.

- (1) Measure the cutting path CP and the needle tip deflection  $\omega_0$  from the ultrasound images.
- (2) Solve the following optimal control problem for the current state of the system  $\omega(n)$  to obtain the optimal control sequence  $u^*(k)$ :

minimize

$$\mathcal{J}(n, \omega(n), u(0)) = \sum_{k=0}^{N-1} w_k \mathcal{L}(n+k, \omega_u(k), u(k))$$

$$\text{subject to } \omega_u(k+1) = f(\text{CP}, \omega_0, \omega_u(k), u(k)) \quad (25)$$

$$\text{and } \sum_{k=0}^{N-1} u(k) - U_{\max} \leq 0.$$

- (3) Define the NMPC control command  $\mu_n := u^*(0)$  and use this value as control command in next sampling time.

In Algorithm 6.1,  $w_k, k = 0, \dots, N-1$ , are weights on summands of the cost function. Using the weights, we can penalize the cost function at a certain time or insertion depth. For instance by setting  $w_{N-1} = 1$  and  $w_k = 0$  for  $k = 0, \dots, N-2$ , the focus of the optimization will be on minimizing the error of the needle steering at the final tip position (target point) rather than tracking a certain trajectory at different depths. Also,  $U_{\max}$  is the constraint we put on the number of needle tip rotations. We intend to minimize the number of needle rotations to limit the tissue damage during needle insertion. Typically, during the insertion of needles into a patient, the surgeon limits the number of the needle rotations. This is due to concerns from physicians that increasing the number of needle rotations will lead to a drilling motion which will increase tissue cutting and damage the surrounding tissue. This has been previously investigated [41, 42]. In the proposed approach this has been done in two different ways: (1) By penalizing the control action in the cost function in (23), and (2) By limiting the total

number of rotations in each optimization step. Constraining  $u$  can be also useful for computational reasons because the optimal control problem is easier to solve if the control variable is penalized.

The optimal control problem must be solved multiple times in each iterate of the NMPC procedure. Thus, we need to use an algorithm that is able to find a good enough solution in a reasonable amount of time. Below, we will use simulated annealing (SA) to find a good approximation to the global optimum of the problem. Simulated annealing is a generic probabilistic metaheuristic method for solving bound-constrained optimization problems. The method models the physical process of heating a material and then slowly lowering the temperature to decrease defects, thus minimizing the system energy [43]. In an optimization problem, as the number of possible solutions gets large, it becomes too computationally intensive to check every possible itinerary. SA is effective at tracking down the best possible solution in a specified fixed optimization time [44]. The method can handle nonlinear constrained problems and have been previously used in autonomous robotic path planning [45, 46].

The inputs to the optimization algorithm are the maximum allowable computation time ( $t_c$ ), the initial temperature ( $T_0$ ), and the annealing parameter ( $k$ ). Temperature is a parameter in simulated annealing that affects the algorithm in two ways: (1) Changing the distance of a trial point from the current point, and (2) Changing the probability of accepting a trial point with a higher objective function value. Trial points correspond to the control input. The binary control input sequence is characterized by two components, namely the number of needle rotations and the depths at which the rotations take place.

The simulated annealing algorithm for solving the finite horizon nonlinear optimal control is as follows:

#### Algorithm 6.2.

- (1) Starting from an initial point and an initial temperature, the algorithm generates a random initial point. The distance of the trial point from the current point is chosen using normal probability distribution with a scale depending on the current temperature. Step length is equal to the current temperature, and direction is chosen to be uniformly random.
- (2) The algorithm determines whether the new point is better or worse than the current point. If the new point is better, it becomes the next point. If not, then the algorithm can still make it the next point using the following acceptance probability function:

$$P_a = \frac{1}{1 + \exp\left(\frac{\Delta}{\max(T)}\right)},$$

where  $\Delta$  is the difference between the new and the old cost functions, and  $T$  is the temperature.

- (3) The algorithm lowers the temperature while storing the best point found so far using

$$T = \frac{T_0}{k},$$

where  $k$  denotes the annealing parameter and is chosen to be the same as the iteration number.

- (4) The algorithm stops when the average change in the objective function is small relative to a predefined tolerance, or when it reaches the optimization time limit ( $t_c$ ).

As mentioned previously,  $t_c$  is the computation time of the optimization process. This time is large compared to the sampling period. Also, the computational delay caused by step (2) in Algorithm 6.1 is not negligible and needs to be considered. In the next section, we present a method to compensate for this delay.

## 6.2. Delay compensation

In this section, we employ our needle steering model as a predictor in the NMPC scheme to compensate for the computation delay. Without the delay compensation proposed in the paper, the solution to the optimal control problem and calculation of the required control action (i.e. depth of needle rotation) will be subjected to delay. This means that the robot will not be able to apply the control command on time. For instance, assume the optimal depth to perform a rotation for correcting the needle path is calculated to be 40 mm. However, when the controller wants to apply this command, the needle will be at a depth of 45 mm (because the needle keeps moving while the optimization problem is being solved).

Close scrutiny of Algorithm 6.1 shows that steps (1)–(3) correspond to different physical tasks: ultrasound-based measurements, computing optimal control input, and applying the control to the physical plant. These tasks are operated by individual components, namely, the sensor, the MPC controller, and the plant (see Fig. 2). The idea behind the compensation approach is to run the NMPC controller component with a predefined time offset ( $t_{\max}$ ). This offset causes the controller to compute a control command ahead of time, such that the computed control command value is readily available at the time it is supposed to be applied to the plant. This offset should be chosen larger than the maximal computing time required to solve the optimal control problem ( $t_c$ ). At time  $t_n$ , the optimal control problem is solved with a prediction  $\hat{\omega}(n)$  of the initial value  $\omega(n)$  based on the available sensor measurement at time  $t_n$ . This prediction is performed using the developed needle steering model, which is also used for the NMPC prediction.

In order to perform this prediction, the control commands to be applied to the plant during the computation time interval and have been computed before by the

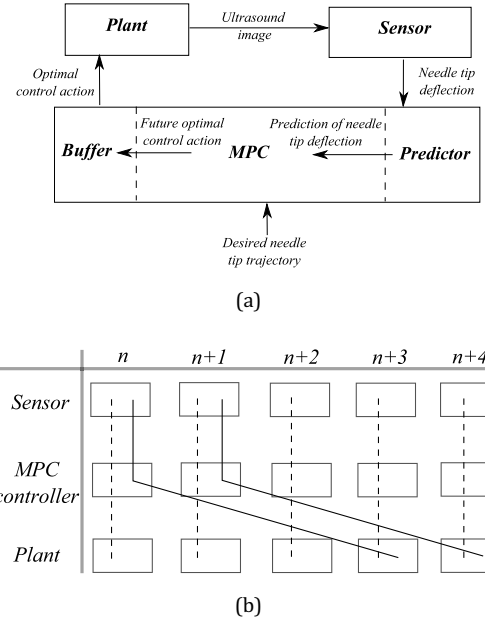


**Fig. 10.** A schematic of the delay compensation strategy. (a) Block diagram of the time decoupled closed-loop NMPC control with delay compensation. (b) Comparison of scheduling structure between NMPC (dashed line) and NMPC with delay compensation with  $t_{\max} = 3 * \text{sampling time}$  (solid line).

NMPC controller are needed to be stored using a buffer. Thus, we extend the scheme given in Fig. 2 by adding the required predictor and buffer to the controller. The structure of the resulting scheme is shown in Fig. 10(a) and the scheduling structure for the delay compensation strategy is sketched in Fig. 10(b). Other than delay compensation, advantage of this method is that we can run the three components of the system as separate algorithms in parallel.

As discussed before, solving step (2) of Algorithm 6.1, is computationally demanding. Thus,  $t_{\max}$  can be relatively larger than the sampling time. Consequently, at the start of the needle insertion for a certain time ( $t_{\max}$ ) no control command will be available. To avoid this situation we solve the optimal control problem offline once before the insertion begins. Then, we use the acquired optimal control command at the beginning of the insertion.

In the next section we present the experiments performed on *ex vivo* tissue phantom to validate the proposed needle steering model and our MPC based needle steering strategy.

## 7. Experimental Evaluation

In this section, needle insertion experiments are designed and performed on soft tissue samples. The goals of the experiments are identifying the model



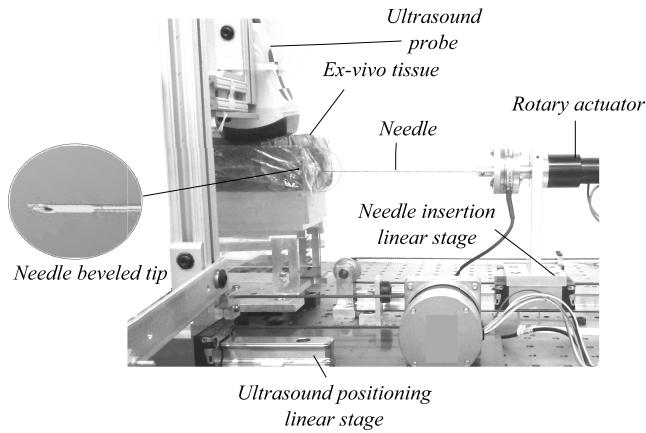


**Fig. 11.** Experimental setup used to perform needle insertion experiments. The setup has three degrees of freedom, the translational and rotational motions of needle and translational motion of the ultrasound probe.

parameters, verifying the model accuracy and validating the proposed needle steering strategy.

In order to perform needle insertion into soft tissue, the setup shown in Fig. 7 is used. The setup consists of a robotic system with three degrees of freedom (DoF). Two DoFs for linear needle insertion and axial needle rotation and one DoF for linear motion of the probe of the ultrasound machine (SonixTouch, Ultrasonix, BC, Canada). During the insertions the ultrasound probe follows the needle tip and acquires transverse images of the needle tip in *ex vivo* tissue. The needle used to perform insertions is a standard 18-gauge brachytherapy needle (Eckert & Ziegler BEBIG Inc., Oxford, CT, USA) made of stainless steel, with an outer diameter of 1.27 mm, an inner diameter of 1 mm. Beef loin tissue is used in the needle steering experiments. Bovine tissue is embedded in gelatin to get a smoother surface on top. This increases the contact surface between the ultrasound probe and the tissue and consequently reduces the noise in the ultrasound images. Same tissue was used in all the experiments.

### 7.1. Model identification and validation

In order to identify the tissue cutting force and the parameters of the soft tissue model, we follow the

approach discussed in our previous work [18]. The values of the parameters of the needle steering model are given in Table 1.

Now, we can validate the model by comparing the predicted and measured needle tip deflection. In the experiments, the brachytherapy needle is inserted to a depth of 135 mm with a speed of 5 mm/s. Experiments are performed with and without axial needle rotation. In insertions with rotation either a single rotation is performed at a depth of 45 and 85 mm, or double rotations are performed at depths of 45 and 85 mm. Five needle insertions are performed for each scenario. A well-tuned PID controller is used to rotate the needle tip in less than 0.2 s as it was inserted, thus ensuring the needle stayed in the insertion plane. Another PID controller is used for ultrasound positioning. Needle tip tracking algorithm discussed in Sec. 5 is used to find the needle tip deflection in the model validation experiments. Settling time of the PID controllers are negligible compared to the delay caused by iteratively solving the optimal control problem.

Figure 13(a) shows the result of needle insertion experiments compared to the model predictions. According to the results, the model captures the effect of axial tip rotation on the needle deflection. The maximum error in predicting the final tip position is 1.24 mm for rotation at the depth of 40 mm. Maximum prediction error for needle tip trajectory is 1.45 mm at the depth of 86 mm for insertion with single rotation at the depth of 80 mm. In model predictions, when the needle is axially rotated, there is a small jump in the needle tip trajectory that corresponds to a sudden change of the cutting force orientation. However, this sudden deflection is small (a maximum of 0.61 mm) and has a negligible effect on the needle tip trajectory predictions. The results of this experiment are summarized in Table 2.

### 7.2. Needle steering results

In this section, needle steering controller is evaluated by performing needle steering experiments in *ex vivo* tissue phantom. Considering the smallest tumour that can be detected using ultrasound images has a diameter of 2.0 mm [2], we considered a circular target region of 2 mm for all the experiments described below. The

**Table 1.** Experimentally identified model parameters and constant known parameters of the model.

Identified parameters	$K_s$ [N/m <sup>2</sup> ]	$C_s$ [N.sec/m <sup>2</sup> ]	$P$ [N]	$Q$ [N]		
	$3.2 \times 10^5$	$9.6 \times 10^4$	0.290	0.798		
Known parameters	$E$ [GPa]	$\ell$ [m]	$\rho$ [Kg/m <sup>3</sup> ]	$A$ [m <sup>2</sup> ]	$I$ [m <sup>4</sup> ]	$\alpha$ [°]
	200	0.2	8030	$4.81 \times 10^{-7}$	$7.75 \times 10^{-14}$	20

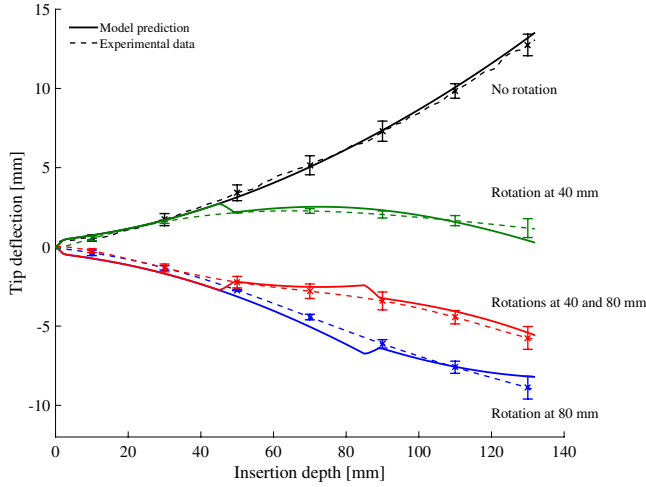


**Fig. 12.** A comparison of experimentally-obtained needle tip deflections and the corresponding model predictions for needle insertion at constant velocity of 5 mm/s with and without axial axial rotations. Error bars denote standard deviation of experimental data.

targeting accuracy of the needle tip is calculated by measuring the distance between the center of the target and the final needle tip position.

The MPC control algorithm is executed on an Intel i7 3.33 GHz PC. The time offset  $t_{\max}$  required for cost function optimization in the MPC, is set equal to 10 s, which is a sufficiently short-time interval for clinical applications that require needle insertion depth ranging from 100 to 150 mm [47]. During the optimization, the needle model is used to generate a minimum of 20 needle trajectory predictions. The needle insertion and rotational velocities used during the experiments are 2 mm/s and 300 rpm, respectively, and the total depth of insertion is 140 mm. In the experiments, the needle tip is inserted in the tissue for 5 mm by hand prior to robotic needle insertion to fix the entry point.

**Table 2.** Results of insertion of the needle with and without axial rotation(s). Final tip position in the experiments  $\omega_{\exp}(\ell)$ , final tip position in the simulation  $\omega_{\text{sim}}(\ell)$ , maximum tip error  $e_{\max}$ , standard deviation of final tip position  $\sigma(\ell)$ , and root-mean-square error (RMSE) are listed. RMSE is calculated as  $\sqrt{\frac{\sum_{i=1}^n (\hat{y}_i - y_i)^2}{n}}$  and is used as a measure of the differences between values predicted by the identified model,  $\hat{y}$ , and the values actually observed in the experiments,  $y$ , for  $n$  data points.

Rotation depth(s) [mm]	—	40	80	40 & 80
$\omega_{\exp}(\ell)$ [mm]	13.52	-0.21	8.29	6.30
$\omega_{\text{sim}}(\ell)$ [mm]	13.06	1.03	9.02	5.85
$e_{\max}$ [mm]	0.43	1.24	1.45	1.29
$\sigma(\ell)$ [mm]	0.69	0.85	0.91	1.06
RMSE [mm]	0.086	0.276	0.462	0.395

Two virtual scenarios are used in the experiments and we executed our system five times for each experimental scenario.

- **Scenario I.** The needle is steered to follow a straight line and reach a target placed at the depth 140 mm. This is similar to the needle insertion in brachytherapy where the seeds should be placed along a straight line within the tissue.
- **Scenario II.** A 4-mm circular obstacle is positioned at 70 mm between the needle entry point in the tissue and the target. The needle is steered to reach a target at the depth of 140 mm while avoiding the obstacle. Obstacles are sensitive or impenetrable anatomical regions in the proximity of the target point such as blood vessels.

In the first scenario, the model prediction horizon is set to 10 s corresponding to insertion depth of 20 mm. In the first scenario, the needle is inserted at a constant velocity of 2 mm/s and the model prediction horizon is set to 10 s corresponding to the insertion depth of 20 mm. Goal of the first scenario is to steer the needle on a straight line and we want the controller to focus on minimizing the trajectory tracking error regardless of the target position. It is clear that by tracking a straight line leading to the target we will be able to reach the target. In the second scenario, the prediction horizon is the maximum insertion depth, i.e. 70 s for insertion depth of 140 mm. The goal of the second scenario is to steer the needle to reach a target at the depth of 140 mm while avoiding an obstacle placed at the depth of 70 mm. In this scenario, we plan to follow a curve going around the obstacle and reaching the target and minimize the targeting error. Thus, in this scenario we select the prediction horizon equal to the total insertion depth to include the targeting error in the optimal control problem. The desired tip trajectory is a third order polynomial starting from the entry point and ending at the target location with maximum distance of 3 mm from the centroid of the obstacle. The number of allowable rotations in the prediction horizon ( $U_{\max}$ ) is three for both scenarios.

A representative results for scenarios I and II are given in Figs. 13(a) and 13(b), respectively. The experimental results are provided in Table 3. The maximum, mean and standard deviation of targeting error are reported.

The maximum targeting error in the first and second scenario are 2.10 and 2.85 mm, respectively. Also, the minimum distance from the obstacle in the second scenario is 1.4 mm. Currently, average seed placement errors by experienced brachytherapists are in the range of about 6.3 mm [5, 48]. Another study showed that prostate biopsies via rigid needles show average targeting errors of 5.5–6 mm [49]. Thus, with the proposed needle steering strategy targeting accuracy can be improved by almost 50%.

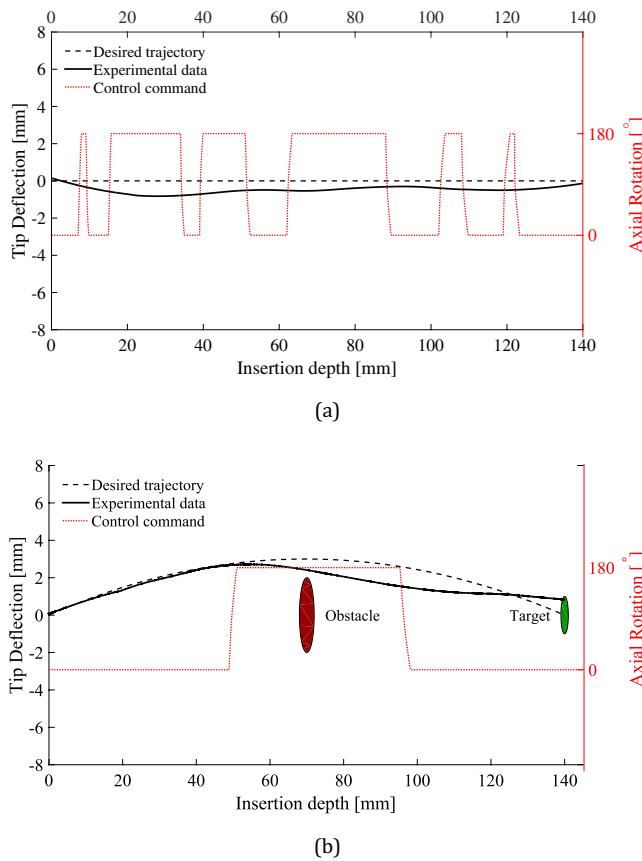


**Fig. 13.** Representative experimental needle steering results and corresponding controller input command (a) Scenario I: needle steering with the aim of moving on a straight line. (b) Scenario II: needle steering with the aim of manoeuvring around an obstacle.

**Table 3.** Result of needle steering experiments. Maximum number of axial rotations  $rot$ , mean targeting error  $e_{mean}$ , maximum targeting error  $e_{max}$ , standard deviation of targeting error  $\sigma$  are listed.

	$rot$	$e_{max}$ [mm]	$e_{mean}$ [mm]	$\sigma$ [mm]
Scenario I	13	2.10	1.75	0.61
Scenario II	7	2.85	2.25	0.97

## 8. Concluding Remarks

This study combines a needle deflection model, image processing techniques, and a MPC to accurately steer bevel tipped flexible needles with the aim of reaching desired target location inside soft tissues.

We proposed a novel model of needle steering dynamics that can be used to predict needle tip deflection in real-time. The model accepts the axial needle rotation as an input and accounts for the effects of tissue deformation during needle insertion. Experimental results demonstrate that the proposed model can predict needle

deflection with a maximum error of 1.45 mm. A needle tip tracking system is developed to determine needle tip deflection from the ultrasound images in real time. The estimated tip deflection is later employed in the needle deflection model to predict needle tip trajectory in the future steps.

The proposed image processing algorithm combined with the needle deflection model make the foundations of a MPC for needle steering. The needle steering controller provides accurate targeting while avoiding anatomical obstacles such as sensitive or impenetrable structures. We experimentally evaluated our approach by performing needle insertion experiments in *ex vivo* tissue. The experimental results demonstrate that our needle steering approach successfully guides the needle to desired targets with and without the presence of obstacles with an average error of less than 2 and 3 mm, respectively, which is within clinically acceptable thresholds.

Identified values for some of the needle steering model parameters (such as the tissue cutting force and tissue stiffness) are only the nominal values and the magnitude of these parameters might change during the needle insertion due to factors such as tissue inhomogeneity. Using the proposed feedback controller, we are able to correct uncertain perturbations caused by deviation of parameters from their nominal values. However, there are new MPC methods with enhanced robustness properties. In future work, we will implement these methods to enhance performance of the needle steering controller.

The main drawback of the proposed system is 2D needle steering. During clinical needle steering the needle tip might deviate and deflect out of plane. Many factors such as tissue inhomogeneity can cause out-of-plane needle deflection. In future work, we will extend the model to capture needle deflection in 3D and perform controlled needle steering in a 3D environment. Also, we intend to enhance the computational efficiency of the model to decrease the time needed for path planning. This way we will be able to perform rapid path planning during the needle insertion. The planner uses the model and the online needle deflection feedback to update the desired trajectory online. Also, in order to provide a more realistic testing scenario, needle steering tests will be conducted on biological tissue with moving targets. In this case, motion of the target can be tracked in the ultrasound images or compensated in the control algorithm using a soft tissue model that predicts target displacements.

## Acknowledgments

This work was supported by the Natural Sciences and Engineering Research Council (NSERC) of Canada under grant CHRP 446520, the Canadian Institutes of Health

Research (CIHR) under grant CPG 127768 and the Alberta Innovates — Health Solutions (AIHS) under grant CRIO 201201232. The authors would like to acknowledge Michael Waine for his assistance with the real-time image processing system used in the paper.

## References

1. N. Abolhassani, R. Patel and M. Moallem, Needle insertion into soft tissue: A survey, *Med. Eng. Phys.* **29**(4) (2007) 413–431.
2. P. Moreira and S. Misra, Biomechanics-based curvature estimation for ultrasound-guided flexible needle steering in biological tissues, (2014) 1–11.
3. D. Rucker, J. Das, H. Gilbert, P. Swaney, M. Miga, N. Sarkar and R. Webster, Sliding mode control of steerable needles, *IEEE Trans. Robotics* **29** (2013) 1289–1299.
4. S. Patil, J. Burgner, R. Webster and R. Alterovitz, Needle steering in 3D via rapid replanning, *IEEE Trans. Robotics* **30** (2014) 853–864.
5. G. J. Vrooijink, M. Abayazid, S. Patil, R. Alterovitz and S. Misra, Needle path planning and steering in a three-dimensional non-static environment using two-dimensional ultrasound images, *Int. J. Robotics Res.* (2014).
6. S. DiMaio and S. Salcudean, Needle steering and model-based trajectory planning, *Med. Image Comput. Computer-Assisted Intervention — MICCAI 2003*, Vol. 2878 (Springer, Berlin Heidelberg, 2003), pp. 33–40.
7. S. DiMaio and S. Salcudean, Interactive simulation of needle insertion models, *IEEE Trans. Biomed. Eng.* **52**(7) (2005) 1167–1179.
8. O. Goksel, S. Salcudean and S. Dimaio, 3D simulation of needle-tissue interaction with application to prostate brachytherapy, *Comput. Aided Surgery* **6** (2006) 279–88.
9. D. Glozman and M. Shoham, Image-guided robotic flexible needle steering, *IEEE Trans. Robotics* **23** (2007) 459–467.
10. R. Alterovitz, A. Lim, K. Goldberg, G. Chirikjian and A. Okamura, Steering flexible needles under Markov motion uncertainty, *IEEE/RSJ Int. Conf. Intell. Robots and Syst.* (2005) 1570–1575.
11. R. Webster, N. Cowan, G. Chirikjian and A. Okamura, Nonholonomic modeling of needle steering, *Experimental Robotics IX*, Vol. 21 (Springer, Berlin Heidelberg, 2006), pp. 35–44.
12. W. Park, Y. Liu, Y. Zhou, M. Moses and G. S. Chirikjian, Kinematic state estimation and motion planning for stochastic nonholonomic systems using the exponential map, *Robotica* **26** (2008) 419–434.
13. D. Minhas, J. Engh, M. Fenske and C. Riviere, Modeling of needle steering via duty-cycled spinning, *29th Annual Int. Conf. IEEE Eng. Med. Biol. Soc. (EMBS)*, (2007), pp. 2756–2759.
14. K. Yan, W. S. Ng, K.-V. Ling, Y. Yu, T. Podder, T.-I. Liu and C. W. S. Cheng, Needle steering modeling and analysis using unconstrained modal analysis, *The First IEEE Int. Conf. Biomed. Robotics and Biomechanics*, (2006), pp. 87–92.
15. O. Goksel, E. Dehghan and S. E. Salcudean, Modeling and simulation of flexible needles, *Med. Eng. Phys.* **31**(9) (2009) 1069–1078.
16. A. Asadian, M. Kermani and R. Patel, A compact dynamic force model for needle-tissue interaction, *Annual Int. Conf. IEEE Eng. Med. Biol. Soc. (EMBS)*, (2010), pp. 2292–2295.
17. T. Lehmann, M. Tavakoli, N. Usmani and R. Sloboda, Force-sensor-based estimation of needle tip deflection in brachytherapy, *J. Sensors* **2013** (2013) 10.
18. M. Khadem, B. Fallahi, C. Rossa, R. Sloboda, N. Usmani and M. Tavakoli, A mechanics-based model for simulation and control of flexible needle insertion in soft tissue, *IEEE Int. Conf. Robotics and Automation (ICRA)*, (2015).
19. S. Misra, K. Reed, B. Schafer, K. Ramesh and A. Okamura, Mechanics of flexible needles robotically steered through soft tissue, *Int. J. Rob. Res.* **29**(13) (2010) 1640–1660.
20. R. Roesthuis, M. Abayazid and S. Misra, Mechanics-based model for predicting in-plane needle deflection with multiple bends, *4th IEEE RAS EMBS Int. Conf. Biomed. Robotics and Biomechanics* (2012), pp. 69–74.
21. T. Adebare, A. Fletcher and A. Okamura, 3-D ultrasound-guided robotic needle steering in biological tissue, *IEEE Trans. Biomed. Eng.* **61** (2014) 2899–2910.
22. S. Misra, K. Reed, A. Douglas, K. T. Ramesh and A. Okamura, Needle-tissue interaction forces for bevel-tip steerable needles, *2nd IEEE RAS EMBS Int. Conf. Biomed. Robotics and Biomechanics, 2008. BioRob 2008* (2008), pp. 224–231.
23. K. Reed, V. Kallem, R. Alterovitz, K. Goldberg, A. Okamura and N. Cowan, Integrated planning and image-guided control for planar needle steering, *2nd IEEE RAS & EMBS Int. Conf. Biomed. Robotics and Biomechanics, BioRob 2008* (2008), pp. 819–824.
24. P. Hagedorn and A. DasGupta, *Vibrations and Waves in Continuous Mechanical Systems* (Wiley, 2007).
25. Y. Fung, *Foundations of Solid Mechanics*. Prentice-Hall international series in dynamics (Prentice-Hall, 1965).
26. B. Galerkin, Series solution of some problems of elastic equilibrium of rods and plates, *Wjestnik Ingenerow Petrograd* (1915) 897–908.
27. G. Genta, *Vibration Dynamics and Control* (Springer, 2009).
28. Z. Wei, L. Gardi, D. Downey and A. Fenster, Oblique needle segmentation for 3D trus-guided robot-aided transperineal prostate brachytherapy, *IEEE Int. Symp. Biomed. Imaging: Nano to Macro* (2004), pp. 960–963.
29. P. M. Novotny, J. A. Stoll, N. V. Vasilyev, P. J. Del Nido, P. E. Dupont and R. D. Howe, GPU based real-time instrument tracking with three dimensional ultrasound, *Med. Image Anal.* **11**(5) (2007) 458–464.
30. H. Neshat and R. Patel, Real-time parametric curved needle segmentation in 3D ultrasound images, *2nd IEEE RAS EMBS Int. Conf. Biomed. Robotics and Biomechanics (BioRob)* (2008), pp. 670–675.
31. M. Ding, Z. Wei, L. Gardi, D. B. Downey and A. Fenster, Needle and seed segmentation in intra-operative 3D ultrasound-guided prostate brachytherapy, *Ultrasonics* **44** (2006) 331–336, *Proc. Ultrasonics Int. World Congress on Ultrasonics (WCU)*.
32. M. Uhercik, J. Kybic, H. Liebgott and C. Cachard, Model fitting using ransac for surgical tool localization in 3D ultrasound images, *IEEE Trans. Biomed. Eng.* **57**(8) (2010) 1907–1916.
33. S. H. Okazawa, R. Ebrahimi, J. Chuang, R. N. Rohling and S. E. Salcudean, Methods for segmenting curved needles in ultrasound images, *Med. Image Anal.* **10** (2006) 330–342.
34. M. Kaya and O. Bebek, Needle localization using gabor filtering in 2D ultrasound images, *IEEE Int. Conf. Robotics and Automation (ICRA)*, (2014), pp. 4881–4886.
35. J. Carriere, C. Rossa, N. Usmani, R. Sloboda and M. Tavakoli, Needle shape estimation in soft tissue based on partial ultrasound image observation, *IEEE Int. Conf. Robotics and Automation (ICRA)*, (2015), pp. 2277–2282.
36. M. Abayazid, G. Vrooijink, S. Patil, R. Alterovitz and S. Misra, Experimental evaluation of ultrasound-guided 3D needle steering in biological tissue, *Int. J. Comput. Assisted Radiol. Surg.* **9**(6) (2014) 931–939.
37. M. Waine, C. Rossa, R. Sloboda, N. Usmani and M. Tavakoli, 3D shape visualization of curved needles in tissue from 2D ultrasound images using ransac, *IEEE Int. Conf. Robotics and Automation (ICRA)*, (2015).
38. S. Smith and J. Brady, SUSAN — a new approach to low level image processing, *Int. J. Comput. Vision* **23**(1) (1997) 45–78.
39. S. J. Qin and T. A. Badgwell, A survey of industrial model predictive control technology, *Contr. Eng. Practice* **11**(7) (2003) 733–764.
40. L. Grne and J. Pannek, *Nonlinear Model Predictive Control* (Springer, London, 2011).



41. P. Swaney, J. Burgner, H. Gilbert and R. Webster, A flexure-based steerable needle: High curvature with reduced tissue damage, *IEEE Trans. Biomed. Eng.* **60**(4) (2013) 906–909.
42. T. Podder, D. Clark, D. Fuller, J. Sherman, W. Ng, L. Liao, D. Rubens, J. Strang, E. Messing, Y. Zhang and Y. Yu, Effects of velocity modulation during surgical needle insertion, *27th Annual Int. Conf. Eng. Med. Biol. Soc., 2005. IEEE-EMBS 2005* (2005), pp. 5766–5770.
43. I. O. Bohachevsky, M. E. Johnson and M. L. Stein, Generalized simulated annealing for function optimization, *Technometrics* **28** (1986) 209–217.
44. V. Cerny, Thermodynamical approach to the traveling salesman problem: An efficient simulation algorithm, *J. Optimization Theor. Applications* **45**(1) (1985) 41–51.
45. W. Carriker, P. Khosla and B. Krogh, Path planning for mobile manipulators for multiple task execution, *IEEE Trans. Robotics and Automation* **7** (1991) 403–408.
46. P. Caricato and A. Grieco, Using simulated annealing to design a material-handling system, *IEEE Intell. Syst.* **20** (2005) 26–30.
47. T. Podder, D. Clark, D. Fuller, J. Sherman, W. Ng, L. Liao, D. Rubens, J. Strang, E. Messing, Y. Zhang and Y. Yu, Effects of velocity modulation during surgical needle insertion, *27th Annual Int. Conf. Eng. Med. Biol. Soc., IEEE-EMBS* (2005), pp. 5766–5770.
48. R. Taschereau, J. Pouliot, J. Roy and D. Tremblay, Seed misplacement and stabilizing needles in transperineal permanent prostate implants, *Radiother. Oncol.* **55**(1) (2000) 59–63.
49. P. Blumenfeld, N. Hata, S. DiMaio, K. Zou, S. Haker, G. Fichtinger and C. M. Tempany, Transperineal prostate biopsy under magnetic resonance image guidance: A needle placement accuracy study, *J. Magn. Reson. Imaging* **26**(3) (2007) 688–694.



**Mohsen Khadem** received his BSc and MSc degrees in Mechanical Engineering from Shiraz University and Sharif University of Technology, Iran, in 2010 and 2013, respectively. He is currently working towards the Doctoral degree in Electrical and Computer Engineering at University of Alberta and is working on robotics-assisted minimally invasive surgery. His current research interests include medical robotics and image-guided surgery.



actuators and sensors technologies, mechatronics, and medical robotics.

**Carlos Rossa** received the Engineering and the MSc degrees in Mechatronics from the Ecole Nationale d'Ingenieurs de Metz, France, both in 2010, and earned the PhD degree in Mechatronics and Robotics from the University of Paris VI, Paris, France in 2013. He is currently a postdoctoral research fellow with the Department of Electrical and Computer Engineering at the University of Alberta, Edmonton, Canada. Dr. Rossa's current research interests include the design and control of haptic interfaces,



**Ron S. Sloboda** is a Professor in Department of Oncology, University of Alberta, Canada. He received his BSc degree in Physics from the University of Manitoba, Canada, in 1974 and his PhD degree in Physics, Nuclear Theory from the University of Alberta, Canada, in 1979. Dr. Sloboda's research interests are dosimetry and treatment planning for brachytherapy, including the design of clinical studies to obtain patient data that inform model-based dose calculation.



**Nawaid Usmani** is an Associate Professor in Department of Oncology, University of Alberta, Canada, and a radiation Oncologist at Cross Cancer Institute, Edmonton, Canada. He received his Bachelor of Arts & Science from McMaster University, Canada in 1998 and his Doctorate of Medicine from McMaster University in 2001. Dr. Usmani's main focus on research is in prostate brachytherapy, including magnetic resonant imaging and PET imaging in the management of prostate cancer.



Robotics (CSTAR), Canada. In 2007–2008, he was an NSERC Post-Doctoral Fellow at Harvard University, USA.

**Mahdi Tavakoli** is an Associate Professor in the Department of Electrical and Computer Engineering, University of Alberta, Canada. He received his BSc and MSc degrees in Electrical Engineering from Ferdowsi University and K.N. Toosi University, Iran, in 1996 and 1999, respectively. He received his PhD degree in Electrical and Computer Engineering from the University of Western Ontario, Canada, in 2005. In 2006, he was a post-doctoral researcher at Canadian Surgical Technologies and Advanced

Dr. Tavakoli's research interests broadly involve the areas of robotics and systems control. Specifically, his research focuses on haptics and teleoperation control, medical robotics, and image-guided surgery. Dr. Tavakoli is the lead author of *Haptics for Teleoperated Surgical Robotic Systems* (World Scientific, 2008).